AD_____

Award Number: DAMD17-97-1-7271

TITLE: A Novel Fuzzy Topological Approach to the Detection of Mammographic Lesions and Qualifications of Parenchymal Density

PRINCIPAL INVESTIGATOR: Jayaram K. Udupa, Ph.D.

CONTRACTING ORGANIZATION: University of Pennsylvania
Philadelphia, Pennsylvania 19104-3246

REPORT DATE: August 1999

TYPE OF REPORT: Annual

PREPARED FOR: U.S. Army Medical Research and Materiel Command
Fort Detrick, Maryland 21702-5012

REPORT DOCUMENTATION PAGE

Form Approved
OMB No. 074-0188

1. AGENCY USE ONLY (Leave blank)	2. REPORT DATE	3. REPORT TYPE AND DATES COVERED
	August 1999	Annual (1 Aug 98 - 31 Jul 99)

4. TITLE AND SUBTITLE
A Novel Fuzzy Topological Approach to the Detection of Mammographic Lesions and Qualifications of Parenchymal Density

5. FUNDING NUMBERS
DAMD17-97-1-7271

6. AUTHOR(S)
Jayaram K. Udupa, Ph.D.

7. PERFORMING ORGANIZATION NAME(S) AND ADDRESS(ES)
University of Pennsylvania
Philadelphia, Pennsylvania 19104-3246

jay@mipg.upenn.edu

8. PERFORMING ORGANIZATION REPORT NUMBER

9. SPONSORING / MONITORING AGENCY NAME(S) AND ADDRESS(ES)
U.S. Army Medical Research and Materiel Command
Fort Detrick, Maryland 21702-5012

10. SPONSORING / MONITORING AGENCY REPORT NUMBER

11. SUPPLEMENTARY NOTES

12a. DISTRIBUTION / AVAILABILITY STATEMENT
Approved for Public Release; Distribution Unlimited

12b. DISTRIBUTION CODE

13. ABSTRACT *(Maximum 200 Words)*

This research focuses on mammographic image processing for the purpose of density quantification, lesion detection and classification. The approaches proposed are different from those taken in the literature in two respects: (1) They emphasize on identifying the dense regions and analyzing their parenchymal architecture. (2) They use a novel fuzzy connectedness method of object definition and image segmentation. During this report period, the following have been accomplished. The development of a novel method of defining the "hanging-togetherness" of dense regions via scale-based affinity and connectedness. An interactive method of lesion segmentation using live wire. An automatic, validated method of mammographic density quantification and the development of a host of intensity-based parameters that are more accurate than the measure of the area of dense regions. A novel method of detecting architectural distortions without explicitly delineating lesions (the method being tested for its effectiveness in predicting the onset of lesions).

14. SUBJECT TERMS
Breast Cancer , Mammographic Image Processing, Lesion Detection, Density Quantification

15. NUMBER OF PAGES
33

16. PRICE CODE

17. SECURITY CLASSIFICATION OF REPORT	18. SECURITY CLASSIFICATION OF THIS PAGE	19. SECURITY CLASSIFICATION OF ABSTRACT	20. LIMITATION OF ABSTRACT
Unclassified	Unclassified	Unclassified	Unlimited

NSN 7540-01-280-5500

Standard Form 298 (Rev. 2-89)
Prescribed by ANSI Std. Z39-18
298-102

FOREWORD

Opinions, interpretations, conclusions and recommendations are those of the author and are not necessarily endorsed by the U.S. Army.

_____ Where copyrighted material is quoted, permission has been obtained to use such material.

_____ Where material from documents designated for limited distribution is quoted, permission has been obtained to use the material.

_____ Citations of commercial organizations and trade names in this report do not constitute an official Department of Army endorsement or approval of the products or services of these organizations.

_na___ In conducting research using animals, the investigator(s) adhered to the "Guide for the Care and Use of Laboratory Animals," prepared by the Committee on Care and use of Laboratory Animals of the Institute of Laboratory Resources, national Research Council (NIH Publication No. 86-23, Revised 1985).

_na___ For the protection of human subjects, the investigator(s) adhered to policies of applicable Federal Law 45 CFR 46.

_na___ In conducting research utilizing recombinant DNA technology, the investigator(s) adhered to current guidelines promulgated by the National Institutes of Health.

_na___ In the conduct of research utilizing recombinant DNA, the investigator(s) adhered to the NIH Guidelines for Research Involving Recombinant DNA Molecules.

_____ In the conduct of research involving hazardous organisms, the investigator(s) adhered to the CDC-NIH Guide for Biosafety in Microbiological and Biomedical Laboratories.

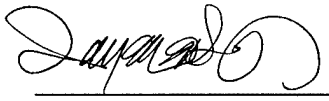

8/24/1999

PI - Signature Date

TABLE OF CONTENTS

INTRODUCTION

Objectives:

This research has the following main aims.

1. To develop and implement a fuzzy object definition method for the detection and delineation of parenchymal density, masses and microcalcifications in digitized mammograms.

2. To develop and implement a fuzzy object definition method for the classification of lesions and mammographic densities.

3. To conduct evaluation studies using histologically verified mammographic data to determine the efficacy of the proposed method of lesion detection and quantitative classifications.

The focus during the report period has been on the following tasks:

Task 4. Conduct evaluation study for single projection lesion detection.

Task 5. Prepare technical report/paper on the work done so far.

Task 6. Implement density classification methods, experiment with affinity relations, verify effectiveness with a few sample data sets, and refine method if needed.

Task 7. Conduct evaluation study for density quantification.

Purpose:

Existing studies on false negative mammograms have found patient age, tumor histology and interpretive variability to contribute to false negative diagnosis. However, breast density appears to be the primary cause of missed carcinomas. The radiographic appearance of female breast differs from woman to woman in relation to the amounts of fat and fibroglandular (connective and epithelial) tissue present. Areas of fat are radiographically lucent while fibroglandular tissues are radiographically dense. There have been many studies looking at the relationship between mammographic density and risk of developing breast cancer. Although a few studies reported no

association with increased risk, the majority of studies have found an association between parenchymal patterns and breast cancer risk. A recent meta-analysis [1] of all studies confirms that subjects with mammographic densities have an increased risk of breast cancer relative to those without densities. The risk increases with the density of the breast [2]. The Wolfe classification was proposed many years ago to identify groups of women at high risk for breast cancer [3]. This scheme was widely used for many years, but has fallen into disuse because of several limitations. For example, inter-observer variability is a problem when the radiologists' subjective assessment is used to classify the amount of density present [4]. Secondly, the magnitude of the increased risk has varied widely in the published studies [1]. Thirdly, identification of this risk factor for a given woman has not altered screening recommendations [5, 6]. Recently a computer-assisted user-interactive method to quantify mammographic density has been published [5], which concluded that quantitative classification of densities allows for more specific gradients of risk than do Wolfe's classifications.

An objective, repeatable quantitative measure of risk derived from mammographic densities will be useful in recommending an alternative screening process. An architecture dependent quantitative analysis of the mammographic densities will make the screening process more effective. Image processing efforts toward this goal seem to be very sparse in the literature, and automatic and efficient methods for generating this measure do not seem to exist.

The focus of this research is on utilizing and extending recently developed fuzzy connectedness method [7] to fulfill the main objectives. This methodology has been successfully applied in several applications including multiple sclerosis lesion detection [8-12], MR angiography [13] and craniofacial soft tissue imaging [14]. The approach of integrating density-derived

information (total density and architecture) into the lesion detection method will hopefully further improve this accuracy.

Scope:

Computer-assisted analysis of mammography density would provide an objective, quantitative measure of cancer risk factor. This measure will be useful in total risk analysis in several ways. First, such risk analysis could influence the choice of alternative screening paradigms such as intervals between mammograms or use of other modalities such as MRI. Second, this measure could be useful in selecting a group of women for whom the risk-benefit ratio of a potentially toxic preventive measure, such as tamoxifen, would be favorable [15, 16]. Third, this measure could be used to signal the need for more careful interpretation of a subset of mammograms. For example, double-reading might be indicated for mammograms above a certain level of density. Fourth, a variety of computer-assisted techniques continue to be developed for mammographic lesion detection. No single algorithm is optimal for all mammograms. Objective density quantification could be helpful for selecting the most appropriate computerized method, or as we propose here for tailoring a selected algorithm. Clearly, an automatic, accurate, and objective method for density quantification will allow the study of the effect of this variable on the implementation of mammograms.

METHODS

Task 4:

During the past year, we have been investigating several methods for the delineation of lesions in digitized mammograms. W have basically pursued two types of approaches.

The first approach is based on fuzzy connectedness. It looks for abnormality in the network by high-strength-of-connectedness paths within the image. The strength of connectedness of every

connecting path between every pair of pixels is determined using the method described in [17]. This method is near the final stages of its development and needs some further work. There are many avenues here which we did not realize earlier. This approach seems to offer, without having to explicitly detect and delineate lesions, a method to identify architectural distortions. One exciting possibility is to determine if sufficient distortion in architecture can be detected well ahead of the time of appearance of visible lesions. We are investigating this avenue currently.

The second approach we have developed is called live wire [18]. In this method, an operator initially selects a point in the vicinity of a lesion boundary. At this time a "live wire" is displayed in real time as the operator moves the mouse cursor. The live wire represents the best path from the initial point selected by the operator to the current cursor position. Since the best path is always computed and displayed in real time, the user can test how to select a largest possible boundary segment by moving the cursor close to the boundary and checking how well the live wire snaps onto the boundary. If this boundary segment is acceptable, the user deposits the cursor which now becomes the new initial point and the process continues. Typically 2-3 points selected on the boundary in this fashion are adequate to segment an entire boundary. A 3D version of this method has also been developed [19] for segmentation of lesions in MR images. This method has also been utilized in other applications [20, 21].

Task 5:

We have so far written 8 papers, four full conference papers and four journal papers, reporting the results of this investigation. We have also presented the results at four conferences. One patent application has also been filed. These are listed later in this report.

Tasks 6, 7:

A method for automatically segmenting dense regions and quantifying density has been fully developed, implemented and tested on over 100 mammograms [22]. The method is described below in some detail.

Segmentation of breast from background: At the very beginning, using 3DVIEWNIX [23] supported LIVE-WIRE [18] tool, regions corresponding to pectoral muscles are interactively excluded when those are projected in the image. In the entire process, this is the only step requiring operator intervention. Fuzzy connectivity is used as the underlying technique in segmenting breast from background. To apply the fuzzy connectivity model, we need to estimate different parameters. Studying 120 images from 60 patients, we found that the intensity histogram always contains a highly prominent peak at the lower intensities, and that peak is contributed mostly by background. The first prominent peak in the intensity histogram is detected and used to (roughly) calculate the mean and standard deviation of background intensity. To apply the fuzzy connectivity algorithm, we need to select a set of reference (seed) pixels. For this purpose, we assume that the rightmost column in the image always lies in the background. We include all these pixels in the reference set. Fuzzy connectedness processing starting from these pixels gives us a fuzzy connectivity image for background. We discard connectivity strengths in the upper half and keep the lower half as the breast region.

Fuzzy connectivity image for glandular tissue: The fuzzy connectivity method is used to enhance glandular dense regions and to suppress fat tissues; the resulting fuzzy connectivity image, in turn, is used for automatic segmentation of the glandular region. The major task in applying the fuzzy connectivity model is to estimate the parameters of the algorithm and to select the set of reference pixels. After ignoring the upper 0.01 percentile intensities, the mean and standard deviation parameters (for the homogeneity and feature-based affinity) are estimated from those parts of the breast region falling in the upper 25% of the intensity range. Finally, the pixels in the breast region falling in the upper 15% of the intensity range are selected as reference pixels. The fuzzy connected image for the glandular tissue is then computed.

Automatic threshold selection: For any threshold, the image is divided into two regions. Local homogeneity based affinity between every pair of spatially adjacent pixels is used to define their likeliness of belonging to the same object or of not belonging to the same object. The optimum

threshold is determined from the associated statistics called threshold energy. The threshold with the minimum threshold energy is selected as the optimum threshold. We generate several descriptors from the segmented binary image and the original image to quantify the glandular tissues as described below. Note that all steps are completely automatic except the exclusion of pectoral muscles if they are included in the mammogram.

Density quantification: The method has been tested on over 80 studies (each study produces two digitized mammograms) from routine exams from two projections (CC and MLO). The images were scanned on a Lumisys scanner at a resolution of 100 microns. The population included normal as well as cancer cases (masses and calcifications). Except the exclusion of pectoral muscles, the entire method has worked automatically on all images wherein all parameters required by the algorithms are selected automatically. The algorithms produced visually acceptable segmentations in all images. From the segmented regions and the image intensities in them, we compute a set of density related parameters including total glandularity(TG), TG/total fat(TF), TG/average fat(AvF), TG/area of breast(AB), area of glandularity(AG), AG/area of fat(AF), AG/AB. TG and TF are computed by integrating radiographic intensity over respective segmented regions while AG, AB and AF are computed by counting the number of pixels in the respective regions. Finally, AvF is computed by dividing TF by AF.

To evaluate the density quantification method, we tested the correlation between the parameters from the two projections (CC and MLO). The correlations for TG, TG/TF, TG/AvF, TG/AB, AG, AG/AF and AG/AB are 0.967, 0.902, 0.951, 0.944, 0959, 0.915 and 0.941, respectively.

We also conducted a phantom experiment as follows. A rectangular parallelepiped wax object was suspended in a cylindrical water bath and imaged at different orientations. The various measures based on integrating intensity in the segmented object (wax) region produced more accurate density quantification than the area measures.

Task 8:

This task has to do with writing papers on density quantification and actually belongs to Year 3, but has been completed based on the density quantification work done so far. See list of papers below.

KEY RESEARCH ACCOMPLISHMENTS

- The development of a novel method of defining the "hanging-togetherness" of dense regions via scale-based affinity and connectedness [17].
- An interactive method of lesion segmentation using live ire [18, 19].
- An automatic, validated method of mammographic density quantification and the development of a host of intensity-based parameters that are more accurate than the measure of the area of dense regions.
- A novel method of detecting architectural distortions without explicitly delineating lesions (the method being tested for its effectiveness in predicting the onset of lesions).

REPORTABLE OUTCOMES

The following papers/patents have been presented, submitted or published.

1. P.K. Saha and J.K. Udupa: "Scale-based fuzzy connectivity: A novel image segmentation methodology and its validation, " *SPIE Proceedings* 3661:246-257, 1999.
2. P.K. Saha and J.K. Udupa: "Scale-based fuzzy connected image segmentation: Theory, algorithms and validation," *Computer Vision and Image Understanding*, accepted.
3. P.K. Saha, J.K. Udupa, E.F. Conant and D.P., Chakraborty: "Near-automatic segmentation and quantification of mammographic glandular tissue density," *SPIE Proceedings* 3661:266-276, 1999.
4. P.K. Saha, J.K. Udupa, E. Conant, D.P. Chakraborty and D. Sullivan; "Breast tissue glandularity quantification via digitized mammograms," *IEEE Transactions on Medical Imaging*, submitted.
5. A.X. Falcao, J.K. Udupa and F.K. Miyazawa: "Ultrafast user-steered segmentation paradigm: Live-wire-on-the-fly," *SPIE Proceedings* 3661:184-191, 1999.
6. A.X. Falcao, J.K. Udupa and F.K. Miyazawa: "An ultrafast user-steered image segmentation paradigm: Live-wire-on-the-fly," *IEEE Transactions on Medical Imaging*," accepted.
7. A.X. Falcao and J.K. Udupa: "Segmentation of 3D objects using live wire," *SPIE Proceedings* 3034:228-235, 1997.

8. A.X. Falcao and J.K. Udupa: "A 3D generalization of user-steered live wire segmentation," *Medical Image Analysis*, accepted.

9. P.K. Saha and J.K. Udupa: "A scale-based fuzzy connectedness method for object segmentation in images," US Patent, submitted.

CONCLUSIONS

1. The new scale-based fuzzy connectedness method is more robust and effective than the original method. It is very effective for mammographic image segmentation.

2. Glandularity is considered to be one of the strongest factors for breast cancer. Automatic breast glandularity quantification from digitized mammograms is practical using the proposed method. The method removes the subjectivity inherent in interactive threshold selection techniques currently used.

3. The live wire method is effective in segmenting mammographic lesions. It seems to be more robust than the active contour methods commonly used. Its utility is being evaluated in 2D (mammographic) and 3D (MRI) lesion segmentation.

4. The fuzzy connectedness method facilitates various ways of characterizing the architecture of the breast. There are some indications that the distortions in architectures as measured by fuzzy connectedness parameters may predict the occurrence of visible lesions. This is being tested at present.

REFERENCES

1. E. Warner et. al.: "The risk of breast-cancer associated with mammographic parenchymal patterns: A meta-analysis of the published literature to examine the effect of method of classification," *Cancer Detection and Prevision* 16(1):67-72, 1992.
2. A.M. Oza and N.F. Boyd: "Mammographic parenchymal patterns: A marker of breast cancer risk," *Epidemiologic Reviews* 15(1):196-208, 1993.
3. J.N. Wolfe: "Risk for breast cancer development determined by mammographic parenchymal pattern," *Cancer* 37(5):2486-92, 1976.
4. M. Moscowitz, P. Gartside and C. McLaughlin: "Mammographic patterns as markers for high-risk benign breast disease and incident cancers," *Radiology* 134(2):293-5, 1980.
5. N.F. Boyd et. al.: "Quantitative classification of mammographic densities and breast cancer risk: Results from the Canadian National Breast Screening Study," *Journal of the National Cancer Institute* 87(9):670-675, 1995.
6. J.N. Wolfe, A.F. Saftlas and M. Salane: "Mammographic parenchymal patterns and quantitative evaluation of mammographic densities: A case control study," *American Journal of Roentgenology* 148(6):1087-92, 1987.
7. J.K. Udupa and S. Samarasekera: "Fuzzy connectedness and object definition: Theory, algorithms and applications in image segmentation," *Graphical Models and Image Processing* 58(3):246-261, 1996.
8. J.K. Udupa, L. Wei, Y. Miki and R.I. Grossman: "A system for the comprehensive analysis of multiple sclerosis lesion load based on MR imagery," *SPIE Proceeding* 3031:610-618, 1997.
9. J.K. Udupa, L. Wei, S. Samarasekera, Y. Miki, M.A. van Buchem and R.I. Grossman; "Multiple sclerosis lesion quantification using fuzzy connectedness principles," *IEEE Medical Imaging* 16(5):598-609, 1997.
10. Y. Miki, R.I. Grossman, J.K. Udupa, M.A. van Buchem, L. Wei, M.D. Phillips, U. Patel, J.C. McGowan and D.L. Kolson: "Differences between relapsing remitting and chronic progressive multiple sclerosis as determined with quantitative MR imaging," *Radiology* 210:769-774, 1999.
11. Y. Miki, R.I. Grossman, J.K. Udupa, L. Wei, M. Polansky. L.J. Mannon, and D.L. Kolson: "Longitudinal analysis of disease burden in relapsing-remitting multiple sclerosis: Lack of correlation between changes in T2 lesion volume and clinical findings," *Radiology*, accepted.

12. A. Kumar, W. Bilker, J.K. Udupa and G. Gottlieb: "Late onset minor and major early evidence for common neuroanatomical substrates detected by using MRI," *Proceedings of the National Academy of Science* 95:7654-7658, 1998.
13. J.K. Udupa, D. Odhner, J. Tian, G. Holland and L. Axel: "Automatic clutter-free volume rendering for MR angiography using fuzzy connectedness," *SPIE Proceedings* 3034:111-119, 1997.
14. J.K. Udupa, J. Tian, D.C. Hemmy and P. Tessier: "A pentium-based craniofacial 3D imaging and analysis system," *Journal of Craniofacial Surgery* 8(5):333-339, 1997.
15. M. Lippman, T.L. Bassford and F.L. Meyskens, Jr.: "A quantitatively scored cancer-risk assessment tool: Its development and use," *Journal of Cancer Education* 7(1):15-36, 1992.
16. T. Chlebowski, et. al.: "Breast cancer chemoprevention. Tamoxifen: Current issues and future prospective," *Cancer* 72(3):1032-7 Supplement, 1993.
17. P. Saha and .J.K. Udupa: "Scale-based fuzzy connected image segmentation: Theory, algorithms and validation," *Computer Vision and Image Understanding*, accepted.
18. A. Falcao, J.K. Udupa and F.K. Miyazawa: "An ultrafast user-steered image segmentation paradigm: Live-wire-on-the-fly," *IEEE Transactions on Medical Imaging*, accepted.
19. A.X. Falcao and J.K. Udupa: "A 3D generalization of user-steered live wire segmentation," *Medical Image Analysis*, accepted.
20. E. Stindel, J.K. Udupa, B.E. Hirsch, D. Odhner and C. Couture: "3D MR image analysis of the morphology of the rear foot: Application to classification of bones," *Computerized Medical Imaging and Graphics*, 23(2):75-83, 1999.
21. E. Stindel, J.K. Udupa, B.E. Hirsch and D. Odhner: "A characterization of the geometric architecture of the peritalar joint complex via MRI: An aid to classification of feet," *IEEE Transactions on Medical Imaging*, accepted.
22. P. Saha, J.K. Udupa, E. Conant, D.P. Chakraborty and D. Sullivan: "Breast tissue glandularity quantification via digitized mammograms," *IEEE Transactions on Medical Imaging*," submitted.
23. J.K. Udupa, D. Odhner, S. Samarasekera, R.J. Goncalves, K. Iyer, K. Venugopal and S. Furuie: "3DVIEWNIX: An open transportable, multidimensional, multimodality, multiparametric imaging system," *Proceedings of SPIE* 2164:58-73, 1994.

Near automatic quantification of breast tissue glandularity via digitized mammograms

Punam K. Saha[a], Jayaram K. Udupa[a], Emily F. Conant[b], Dev P. Chakraborty[c]

[a]Medical Image Processing Group, [b]Breast Imaging Section, [c]Physics Section,
Department of Radiology, University of Pennsylvania, Philadelphia, PA 19104

ABSTRACT

Studies reported in the literature indicate that breast cancer risk is associated with mammographic densities. Although, an objective, repeatable quantitative measure of risk derived from mammographic densities will be of great use in recommending alternative screening paradigms and/or preventive measures, image processing efforts toward this goal seem to be very sparse in the literature, and automatic and efficient methods do not seem to exist. In this paper, we describe and validate an automatic and reproducible method to segment glandular tissue regions from fat within breasts from digitized mammograms using scale-based fuzzy connectivity methods. Different measures for characterizing density are computed from the segmented regions and their accuracies in terms of their linear correlation across two different projections (CC and MLO) are studied. It is shown that quantization of glandularity taking into account the original intensities is more accurate than just considering the segmented areas. This makes the quantification less dependent on the shape of the glandular regions and the angle of projection. A simple phantom experiment is done that supports this observation.

Keywords: Image analysis, mammograms, glandular tissue, image segmentation, connectedness

1. INTRODUCTION

In the mid 1970s, studies by John Wolfe[1,2] suggested that an association existed between mammographic parenchymal patterns and the risk of developing breast cancer. Since then there have been many studies looking at the relationship between mammographic fibroglandular density (briefly, density) and risk of developing breast cancer. Although a few studies reported no association with increased risk, the majority of studies have found an association between parenchymal patterns and breast cancer risk. A recent meta-analysis[3] of all studies confirms that subjects with mammographic densities have an increased risk of breast cancer relative to those without densities. The risk increases with the density of the breast.[4] In is well known that women with dense breasts appear to have a four to six fold increase in breast cancer risk. Cancers are detected at later stages in dense breasts and mammographers recognize that their diagnostic accuracy is lower in such women.

The Wolfe classification was proposed many years ago to identify groups of women at high risk for breast cancer.[5] This scheme was widely used for many years, but has fallen into disuse because of several limitations. For example, inter-observer variability is a problem when the radiologists' subjective assessment is used to classify the amount of density present.[6] Secondly, the magnitude of the increased risk has varied widely in the published studies.[3] Thirdly, identification of this risk factor for a given woman has not altered screening recommendations.[7,8] Recently an computer-assisted user-interactive method to quantify mammographic density has been published,[7] which concluded that quantitative classification of densities allows for more specific gradients of risk than do Wolfe's classifications.

Computer-assisted analysis of mammographic density would provide an objective, quantitative measure of cancer risk factor. This measure will be useful in total risk analysis in several ways. First, such risk analysis could influence the choice of alternative screening paradigms such as intervals between mammograms or use of other modalities such as MRI. Second, this measure could be useful in selecting a group of women for whom the risk-benefit ratio of a potentially toxic preventive measure, such as tamoxifin, would be favorable.[16,17] Third, this measure could be used to signal the need for more careful interpretation of a subset of mammograms. For example, double-reading might be indicated for mammograms above a certain level of density.

Correspondence: Email: saha@mipg.upenn.edu; http://www.mipg.upenn.edu/~saha/index.html; Telephone: 215 662 6780
Fax 215 898 9145

Image processing efforts toward this goal seem to be very sparse in the literature, and automatic and efficient methods for generating this measure do not seem to exist. Boyd et. al.[7] studied the relation between mammographic densities and breast cancer risk using both radiologist classification and computer assisted density measurement. The computer assisted measurement was based on interactive density thresholding using two user selected thresholds. They observed statistically significant increases in breast cancer risk associated with increasing mammographic density in both methods. Boone et. at[18] developed and evaluated a computerized method of calculating a breast density index and compared this index with breast density index ranking provided by mammographers. Byng et. al.[19] made a quantitative symmetry analysis between mammograms of different breasts of the same patient and between mammograms at different projections of the same breast via subjective classification, interactive thresholding, regional skewness measurement and texture analysis. Ursin et. al.[20] studied the change in mammographic densities in women participating in a trial of a gonadotropin-releasing hormone agonist (GnRHA)-based regimen for breast cancer prevention using simultaneous evaluation, expert outlining and non-expert computer-based thresholding methods. They observed that all three methods yielded statistically significant reduction in densities from baseline to the 12-month follow-up mammogram in women on the contraceptive regimen. They found a high correlation between computer-based results and the results from the expert outlining method. Huo et. al.[21] studied the ability of computer extracted features, computed over a region of interest selected from the central breast region, along with age to identify women at risk. They found that a computerized characterization of parenchymal patterns may be associated with breast cancer risk.

In this paper, we describe and validate an automatic and reproducible method to quantify mammographic densities and study the accuracy of related parameters. Further, we show that quantitation of glandularity taking into account the original intensities is more accurate than just considering the segmented area. This makes the measurement less dependent on the shape of the glandular regions and the angle of projection. In Section 2, a brief description of the scale-based fuzzy connectedness principles is presented that forms the core of the proposed method. In section 3, we describe how different parameters are automatically selected for applying fuzzy connectivity on different regions. In Section 4, we discuss the results and validate the method by studying linear correlations of different area and density related parameters obtained from a set of mammograms across two projections and also by a phantom study. We show that quantitation of glandularity taking into account the original intensities is more accurate than just considering the segmented area. Finally, we state our conclusions in Section 5.

2. SCALE-BASED FUZZY CONNECTEDNESS PRINCIPLES

The concepts described here are applicable to n-dimensional (fuzzy) digital spaces; see[22,23] for details. However, since our application deals with 2D images, we confine only to two-dimensional (2D) case.

Most real objects have a heterogeneous material composition. Further, imaging devices have inherent limitations including spatial, parametric, and temporal resolutions. In the acquired images of objects, these introduce inaccuracies and artifacts such as noise, blurring, and background variation. The artifacts together with material heterogeneity cause the object regions to exhibit a gradation of intensity values in the image. Even if the physical object is perfectly homogeneous and is made of exactly one material, its image will exhibit a graded composition within the object regions due to artifacts. In spite of the graded composition, knowledgeable human observers usually do not have any difficulty in perceiving object regions as a gestalt. That is, image elements in these regions seem to hang together to form the object regions in spite of their gradation of values. These two notions — graded composition and hanging togetherness — are addressed by the scale-based fuzzy connectedness methods for defining objects in acquired images.[23] The scale-based method is outlined below to the extent needed to follow our breast segmentation approach. See[23] for details.

Throughout we denote the digitized mammographic image, referred to as a (2D) *scene*, by $C = (C, f)$, where C denotes the pixel array, and $f(c)$ denotes the pixel value for any $c \in C$. The range of f is assumed to be $[L, H]$. We define a fuzzy relation κ, called *fuzzy affinity*, on the pixel array C. This is intended to be a local relation among pixels that are nearby. The strength of this relation between any two pixels c and d in C, denoted by $\mu_\kappa(c, d)$, depends on (1) how far c and d are; (2) how similar the intensity values (or other features) of the pixels in a circular neighborhood around c are to those around d; (3) how close the intensity values (or other features) of the pixels around c and those around d are to some expected values (or features) for the object region under consideration. The idea behind (1) is that to have the notion of a *fuzzy adjacency* — the further two pixels are the less adjacency (and, therefore, affinity) they have. The strength of the fuzzy adjacency relation between any two pixels c and d in

C is denoted by $\mu_alpha(c,d)$. The idea behind (2) is to define a homogeneity-based affinity between nearby pixels c and d. The more homogeneous the regions in which c and d are, the more is their affinity. The idea behind (3) is to define an object-feature-based affinity between nearby pixels c and d. For the object regions, there is some expected value of the intensity (of their features). The closer the values of the pixels in the vicinity of c and d are to this expected value, the greater must be the affinity of c and d. The size of the circular neighborhood is determined by the "scale" at c and d. Scale is a well established concept in image processing. The *object scale* in C at any pixel c in C denotes the size (radius) of the largest disc centered at c that lies entirely in the object region. Ironically, it appears that computing scale requires image segmentation. However, it is possible to develop algorithms that give a rough estimate of object scale at every pixel based on measuring homogeneity discontinuities and not requiring explicit segmentation. We have demonstrated in[23] that, this estimation is sufficient to give a good approximation of the scale and to improve fuzzy-connectedness-based segmentation.

The notion of affinity captures the local hanging-togetherness property of pixels. The notion of fuzzy connectedness expands this into a global phenomenon as follows. Consider any two pixels c and d (not necessarily nearby) in C. Consider any path (i.e., a sequence of nearby pixels) starting from c and ending in d. We define a "strength of connectedness" of this path as simply the smallest affinity (weakest link) along the path between a pair of successive pixels. Fuzzy connectedness is a global fuzzy relation, denoted K, on C. The strength of this relation between c and d (not necessarily nearby), denoted $\mu_K(c,d)$, is the largest of the strength of connectedness of *all possible* paths between c and d. A scale-based fuzzy connected object of C of strength θ that contains a specified pixel o in C is a subset O of pixels of C. O is such that, for any two pixels c,d in O, $\mu_K(c,d) \geq \theta$, and for any pixel e not in O, $\mu_K(c,e) < \theta$. Given C, o, θ and a scale-based affinity relation κ, finding O requires literally the computation of the strength of connectedness of all possible paths between each of the set of all possible pairs of pixels in C. However, the theory leads to practically viable algorithms[22,23] of far less complexity. The method also provides "training" facilities so that the parameters of κ that are suitable for a given application can be determined automatically by painting sample regions in a few image data sets related to the application.

For any scene $\mathcal{C} = (C, f)$, any fuzzy affinity κ, any pixel o, we define the *fuzzy connectivity scene* of $\mathcal{C}$ with respect to o to be the scene $\mathcal{C}_{Ko} = (C, f_{Ko})$, where for any $c \in C$, $f_{Ko}(c) = \mu_K(o,c)$. That is, the value assigned to any pixel c in $\mathcal{C}_{Ko}$ is the strength of connectedness of c and o. We generalize this definition from a single pixel o to set of pixels X by setting $f_{KX}(c) = \max_{x \in X}\{\mu_K(x,c)\}$. That is, in the fuzzy connectivity scene $\mathcal{C}_{KX} = (C, f_{KX})$ of $\mathcal{C}$ with respect to X, any pixel c is assigned a value $f_{KX}(c)$ that is the maximum of the strength of connectivity of c with the elements of X. Connectivity scenes are what are output by the fuzzy connectedness algorithms.[22,23] Upon thresholding them, we get the segmented fuzzy objects.

3. METHODS

Our method of fibroglandular density quantization consists of the following steps: (1) segmentation of the breast region from background; (2) segmentation of fat and glandular regions within the breast; (3) estimation of the density quantification parameters. These are described in separate subsections below.

3.1. Segmentation of Breast from Background

At the very beginning, using 3DVIEWNIX[24] supported live-wire[25] tool, regions corresponding to pectoral muscles are interactively excluded when those are projected on to the scene. This tool takes help from the operator in recognizing where the pectoral muscles are in the image but does the delineation of their boundary automatically. In this fashion, subjectively is minimized. In the entire process of glandularity quantification, this is the only step requiring operator intervention, if pectoral muscles appear in the mammographic projection. Scale-based fuzzy connectivity is used for segmenting the breast region from the background. Our approach will be to segment the background region rather than the breast region. To do this, we need to (1) determine the parameters of the membership function μ_κ of the affinity relation κ for the background; and (2) specify a set of pixels in the background region. These are accomplished automatically as described below.

In this study, we have utilized 120 mammograms from 60 patients, each in two projections — MLO and CC. Studying all the 120 mammograms, we found that intensity histograms of mammograms always contain a highly prominent peak at low intensities, and this mode corresponds to the background. A typical histogram is shown in Figure 1. The first prominent peak in the histogram is detected and the intensity m_b corresponding to this peak is considered as the mean background intensity. Observing that the histogram is roughly symmetric about m_b, the

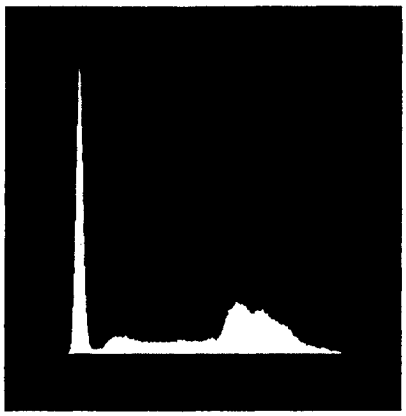

Figure 1. A typical mammographic intensity histogram.

standard deviation of background intensities σ_b is computed as the root-mean-squared distance of the intensities from m_b as follows. Let $h(i)$ represent the number of pixels in the mammographic scene with intensity i (i.e., $h(i)$ is the height of the histogram at i). Then, σ_b is determined as follows

$$\sigma_b = \sqrt{\frac{\sum_{L \leq i \leq m_b} (i - m_b)^2 \, h(i)}{\sum_{L \leq i \leq m_b} h(i)}}. \tag{1}$$

Instead of an operator painting pixels in the background region for training, the set of pixels in C satisfying $L \leq f(c) \leq m_b + 3\sigma_b$ is utilized for estimating the parameters of μ_κ. The exact functional form of μ_κ utilized here is as described in an earlier paper that dealt with the theory and algorithms for the scale-based approach.[23] Since the full description requires a detailed explanation of the concept related to homogeneity-based and object-feature-based affinity, it is not included here. We assume that the top-right and the bottom-right corners in the mammographic scene always lie in the background and include these two pixels in the reference set X for scale-based fuzzy connectedness processing starting from these two pixels gives us a fuzzy connectivity scene for the background. Figure 2(b) shows such a connectivity scene for the mammogram at CC projection shown in Figure 2(a). As shown in Figure 2(b), there is a very good contrast between the background and the breast region. We discard connectivity strengths greater than half the maximum strength and keep the lower half as the zone for the breast region. This zone, however, often includes high noise pixels and markers in the background often used during mammography. To eliminate these pixels, the leftmost 1-pixel on the middle row in the thresholded connectivity scene is chosen as the reference pixel and the hard connected component containing this pixel is found as the breast region. Figure 2(c) shows the hard segmented breast region for the original mammogram of Figure 2(a). This method has worked correctly and automatically in all studies we have analyzed so far.

3.2. Segmentation of Fat and Glandular Regions

Our strategy here is to segment the glandular region as a set of fuzzy connected objects. The segmentation operation is confined to the breast region. The fat region thus gets defined indirectly as the complement of the glandular region in the breast. For this segmentation, as in breast segmentation, we need to specify the parameters of μ_κ as well as a few pixels as the starting information in the glandular region.

Our approach to computing the parameters of μ_κ will be as for the segmentation of the breast region — to determine automatically a set of pixels that are definitely in the glandular region and then to estimate the parameters from the intensity distribution within the set of pixels. To determine this set, the largest intensity value MAX is determined by ignoring the upper 0.1 percentile of intensity in the histogram of the breast region. Similarly, the smallest intensity value MIN is determined by ignoring the lower 0.1 percentile of intensity. We then select within the breast the set of pixels having intensity not less than $MIN + 0.75(MAX - MIN)$ for estimating the parameters of μ_κ. Finally, the set of pixels in the breast region with intensity greater than $MIN + 0.85(MAX - MIN)$ is

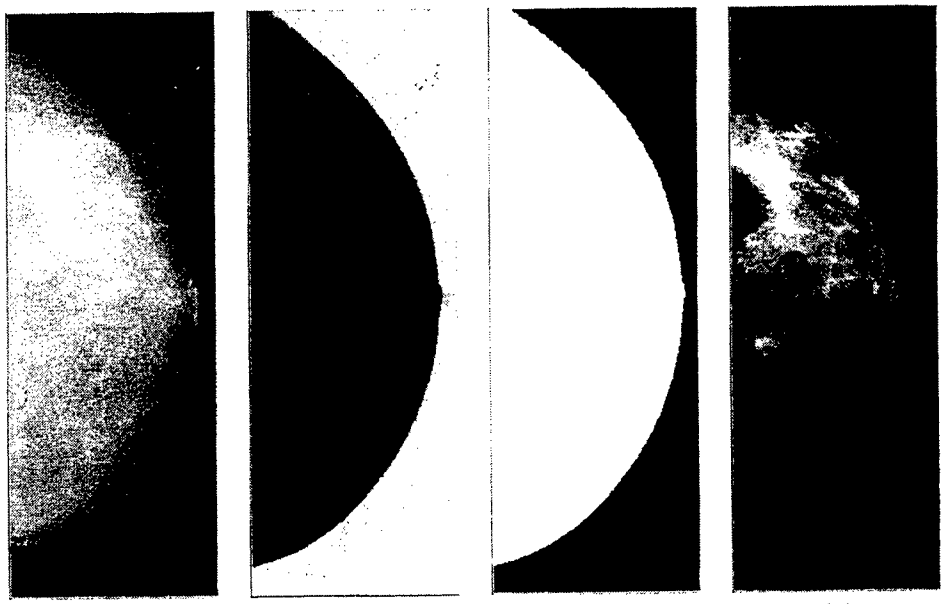

Figure 2. (a) An original mammographic scene for a patient's breast at CC projection. (b) Scale-based fuzzy connectivity scene for the background. (c) Segmented breast region. (d) Scale based fuzzy connectivity scene for the glandular region.

used as the set of reference or seed pixels. Figure 2(d) shows the scale-based fuzzy connectivity scene obtained for the glandular region for the original mammogram in Figure 2(a). In the next section, we describe an automatic threshold selection method that is applied on the fuzzy connectivity scene for a segmentation of the breast region into glandular and fatty regions.

3.3. Automatic threshold selection

In this section, we describe a new automatic threshold selection method for segmenting the glandular regions from the fuzzy connectivity scene. The method is a general threshold selection technique that is applicable to any image, and not necessarily only to connectivity scenes. It optimizes threshold energy computed by considering spatial arrangements of pixel intensities within each region and across regions. We emphasize that the processing is now confined to the breast region. The basic idea is as follows. Every threshold divides the scene into two regions. A second order statistic, threshold energy, of local disagreements in the scene stemming from this partitioning is estimated and is used as a criterion for optimizing the threshold. Threshold energy characterizes the goodness (rather, badness) of a particular threshold and is defined as follows. Let B denote the set of pixels in the segmented breast region. We define two fuzzy relations ρ and $\overline{\rho}$, respectively called *likeliness of belonging to the same object* and *likeliness of belonging to different objects*, on the pixels in B. Strengths of both these relations between any two pixels c and d in B depend on (1) how far c and d are; and on (2) how similar the intensity values (or other features) of the pixels in the circular neighborhood around c are to those around d. As discussed in Section 2, size of the circular neighborhoods around c and d depends on the object scales at c and d. In fact (2) is the measure of homogeneity-based affinity between c and d and its strength is denoted $\mu_\psi(c,d)$ (see[23] for details). Two controlling parameters (indicating expected object homogeneity) are required to calculate the value of the fuzzy relation ψ. These two parameters are estimated as the mean and standard deviation of intensity differences of all pairs of adjacent pixels in the region with pixel intensities (connectedness values) falling in the upper half of the histogram. The strength of the fuzzy relation "likeliness of belonging to the same object" between two pixels $c, d \in B$, denoted $\mu_\rho(c,d)$, is then

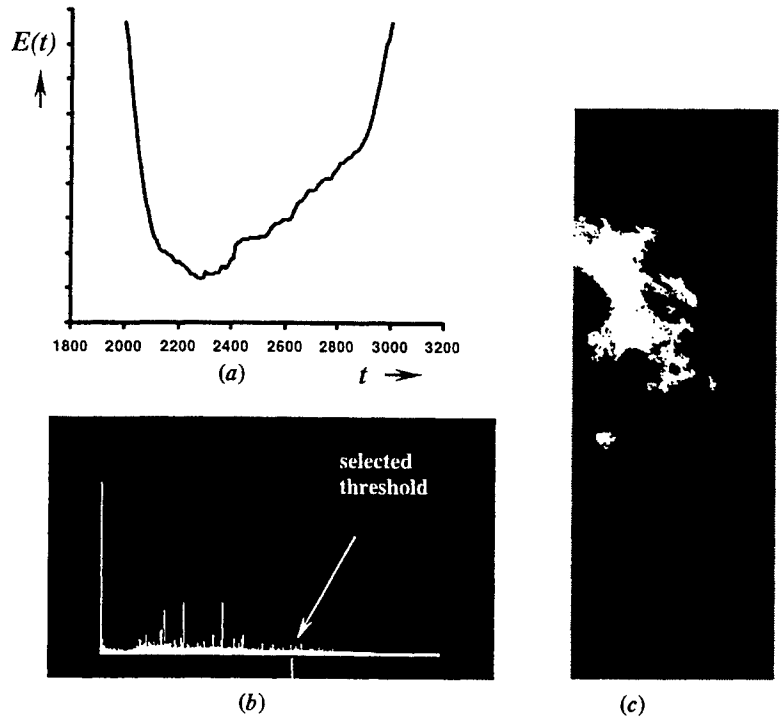

Figure 3. (a), (b) Threshold energy and connectivity strength distributions for the connectivity scene of Figure 2.(d). (c) Segmented glandular region using automatic thresholding.

computed as follows.

$$\mu_\rho(c,d) = \mu_\alpha(c,d)\frac{\sum_{\substack{a,b \in B \text{ s.t.} \\ \mu_\psi(a,b) \le \mu_\psi(c,d)}} \mu_\alpha(a,b)}{\sum_{a,b\in B}\mu_\alpha(a,b)}. \tag{2}$$

The strength of the fuzzy relation "likeliness of belonging to different objects" between two pixels $c, d \in B$, denoted $\mu_{\overline{\rho}}(c,d)$, is computed as follows.

$$\mu_{\overline{\rho}}(c,d) = \mu_\alpha(c,d)\left(1 - \frac{\sum_{\substack{a,b \in B \text{ s.t.} \\ \mu_\psi(a,b) \le \mu_\psi(c,d)}} \mu_\alpha(a,b)}{\sum_{a,b\in B}\mu_\alpha(a,b)}\right). \tag{3}$$

Let $f_p(c,d,t)$ denote a predicate that takes a value '1' when the pixels c, d belong to the same object at the threshold t and '0' otherwise. Then the threshold energy $E(t)$ is determined as follows.

$$E(t) = \sum_{c,d\in B} f_p(c,d,t)\mu_\rho(c,d) + (1 - f_p(c,d,t))\mu_{\overline{\rho}}(c,d) \tag{4}$$

In words, $E(t)$ expresses the level of concordance between the two regions resulting by applying the threshold to the connectivity scene. Finally, the threshold for which $E(t)$ is minimum (indicating minimum concordance or maximum discordance between the two regions) is selected as the optimum threshold. For the fuzzy connectivity scene of Figure 2.(d), distribution of $E(t)$ is shown in Figure 3(a) while Figure 3(b) shows the location of the optimum threshold on the histogram of the connectivity scene of Figure 2(d). The segmented binary scene is shown in Figure 3(c).

3.4. Density Quantification

From the original scene and the segmented fat and glandular regions, the following parameters are computed.

TG: Total glandularity within the breast region computed as the sum of intensities of pixels in the segmented glandular region.

TF: Total fat within the breast region computed as the sum of intensities of pixels in the segmented fat region.

AB: Total area of breast computed as the number of pixels in the segmented breast region.

AG: Total area of glandularity within the breast region computed as the number of pixels in the segmented glandular region.

AF: Total area of fat within the breast region computed as the number of pixels in the segmented fat region.

AvF: Average pixel intensity within the fat area given by TF/AF.

TLG: Total logarithmic glandularity within the breast region computed as the sum of logarithmic values of pixel intensities in the segmented glandular region.

The following parameters, some of which are derived from the above, which may be more meaningful, are actually used in our testing: TG, TG/TF, TG/AvF, TG/AB, AG, AG/AF, AG/AB, and TLG. Linear correlations of each these parameters across two different projections (CC and MLO) were tested for all 60 studies.

4. RESULTS AND DISCUSSION

The Method has been tested in two ways — (1) validation on mammograms at two different projections, and (2) validation on phantoms.

4.1. Validation on Mammograms

The method has been tested on 60 studies selected from our database. Each study had two mammographic projections — CC and MLO. These mammograms were digitized on a Lumisys scanner at a resolution of 100 microns. The population includes normal as well as benign and malignant masses and calcifications. Except for the exclusion of pectoral muscles in some cases, the entire method worked automatically on all mammograms wherein all parameters required by the algorithms were selected automatically. The algorithms produced visually acceptable segmentations in all 120 cases. Figure 4 demonstrates the results of application of the proposed automatic method of tissue glandularity segmentation on several mammograms. The linear correlation coefficients for the parameters TG, TG/TF, TG/AvF, TG/AB, AG, AG/AF, AG/AB, and TLG derived from the two sets of projection images were 0.967, 0.902, 0.951, 0.944, 0.959, 0.915, 0.941 and 0.960, respectively.

The high value of correlation coefficients indicates that our method of measurement is highly consistent between the two projection images of the same patient. The highest correlation is obtained for TG. Generally the parameters that use area measurements yielded lower correlations. This is understandable because, unless the 3D shape of the actual glandular region in the breast is approximately spherical, the shapes of its CC and MLO projections may be quite different from each other. This may yield very different area measures (AG, AF) although the total glandularity may still be the same. To verify these hypothesis, we selected among the 60 pairs of studies a subset in which the shapes of projections of the same breast in CC and MLO appeared quite different. For this subset, we then computed the correlation coefficients. The coefficients for TG and AG for this subset were 0.898 and 0.68, respectively. For the remaining studies, these coefficients were 0.977 and 0.976, respectively. To further verify this hypothesis, we conducted a phantom experiment described below.

4.2. Phantom Study

We affixed, using double-stick tape, a wax rectangular parallelepiped, measuring 0.85 cm × 1.05 cm × 4.6 cm, to the base of a cylindrical container. The latter was filled with water to a height of 5 cm. An image of this phantom was taken on a GE-DMR mammography machine at 27 kVp and 400 mAs. The X-ray beam was directed along the axis of the plastic cylinder which closely corresponded with one of the axes of the wax rectangular parallelepiped. Two more images were then acquired with the parallelepiped tunnel so as to align the other two axes with the beam direction. In this mammer we obtained three orthogonal projections of the wax object. The digitized phantom images are shown in Figures 5.(a)–(c). Since, wax has a lower atomic number than water, it appears darker. It is meant to simulate fatty tissue. The water simulates the glandular tissue. In breast images, the fatty regions surround

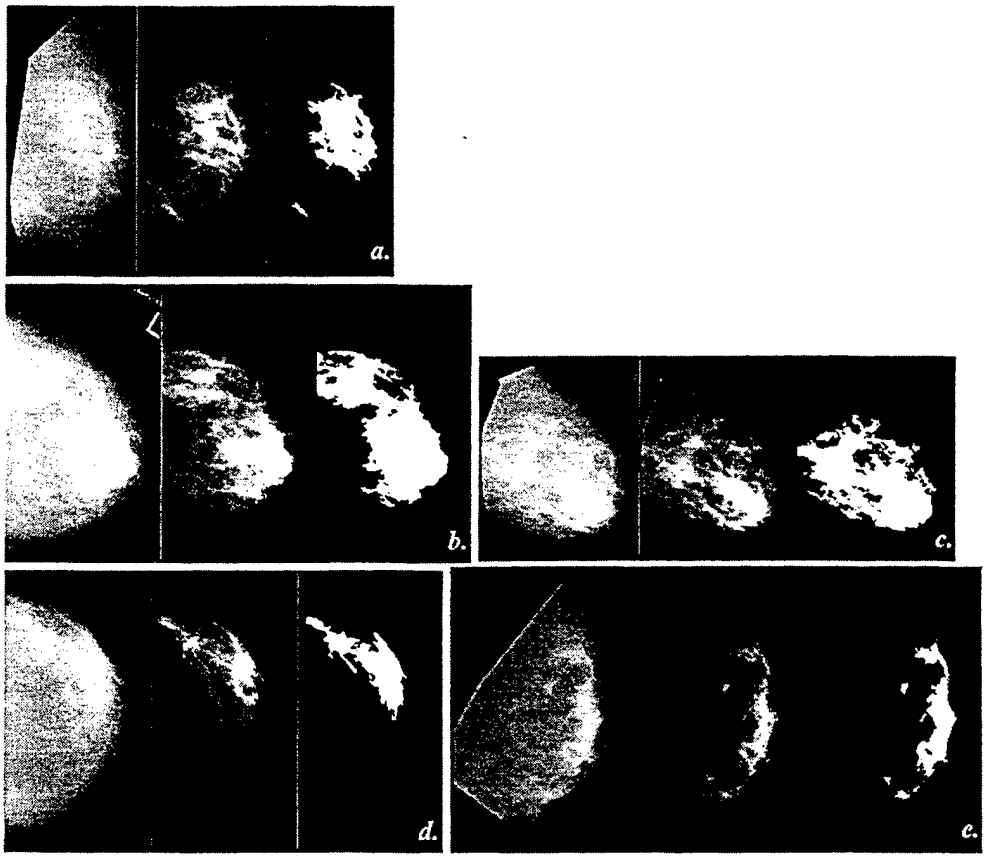

Figure 4. Results of application of the proposed glandularity segmentation method on several mammograms at CC and MLO projections. In each set, the original scene, the connectivity scene for the glandular region and the segmented glandular region are shown.

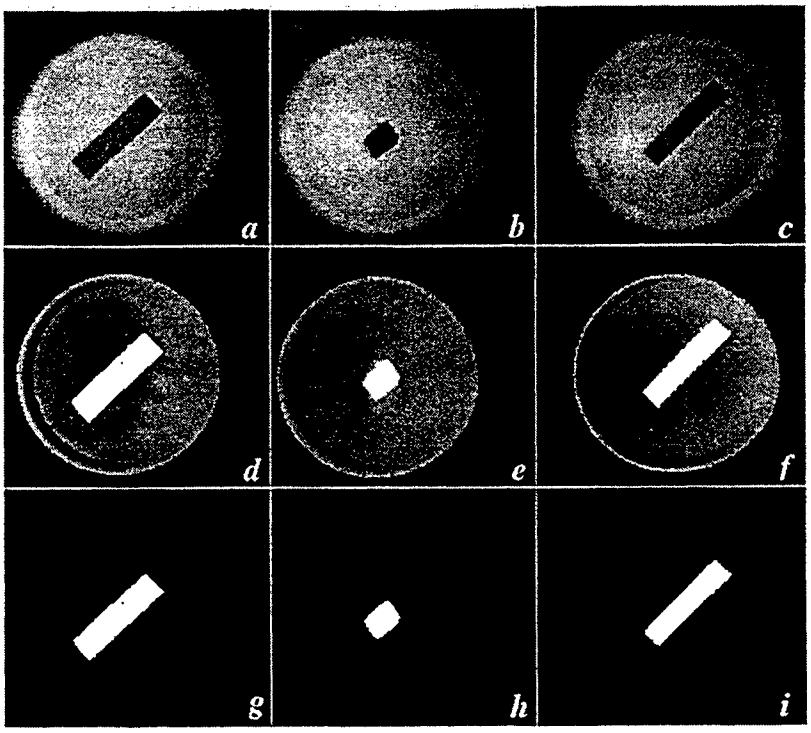

Figure 5. (a)-(c) Phantom images captured at three orthogonal positions of the object. (d)-(f) Fuzzy connectivity scenes. (g)-(i) Segmented object regions from fuzzy connectivity scenes.

the glandular region, but in our simulation the reverse is true. To apply our automatic algorithms, the foreground image containing the projected water and wax regions was negated after segmenting out the background region. Figures 5.(d)–(f) show the fuzzy connectivity scenes for the wax object in the three phantom images. Automatic thresholding was then applied and Figures 5.(g)–(i) show the segmented wax regions. Table 1 shows the value of different parameters computed over the segmented wax and water regions in the three images. Since the average pixel intensity in the wax region (object of interest) is less than that in the surrounding water region, the TLG parameter is computed in a slightly different way by summing the logarithmic values of the ratios of average water pixel value to the pixel intensities over the segmented wax region. From Table 1 we observe that TG is more stable than AG over different projections in the phantom images. In fact, TLG is very stable across the projections and supports our hypothesis that the total object material volume is better captured by integrating the pixel intensities over the segmented region rather than by computing the area of this region. TLG did not show better correlation than TG in patients studies which is perhaps due to the fact that, unlike the phantom, breasts are not composed of two homogeneous materials.

Table 1. Values of different parameters computed over the segmented wax regions in three images.

TG	TG/TF	TG/AvF	TG/AB	AG	AG/AF	AG/AB	TLG	AvF
2128×10^4	0.03117	16671	36.46	48835	0.09132	0.08368	20456	1276
1401×10^4	0.01940	10990	24.07	15509	0.02737	0.02664	20443	1274
2286×10^4	0.03382	17990	39.87	41347	0.07773	0.07212	23863	1270

5. CONCLUSION

A near automatic method for quantification of breast glandularity from digitized mammograms has been developed and tested on 60 pairs of patient mammograms and on a phantom. This method was executed automatically except for the exclusion of projected pectoral muscles. The method consists of the following steps: separation of the breast from the background, creation of a fuzzy connectivity scene for the glandular region, segmenting this connectivity scene using an automatic threshold selection method, and then computing various parameters that characterize total breast glandularity. A set of density and area related parameters has been proposed and their accuracy in terms of their linear correlation across two different projections have been studies. The scale-based fuzzy connectivity method has been found to be quite robust and effective in segmenting the mammographic images. The method seems to be appropriate for characterizing architectural abnormalities. Glandularity is considered to be one of the strongest factors for breast cancer. Automatic repeatable, and consistent breast glandularity quantification from digitized mammograms is practical using the proposed method. The correctness of the proposed glandularity quantification method has been validated by the high R-values of linear correlation between the two projections (CC, MLO) of the various parameters computed over segmented glandular and fatty regions. A simple phantoms experiment was carried out which also supports the results. The method removes the subjectivity inherent in interactive threshold selection techniques currently used. The ability of the computed glandularity parameters in evaluating risk is currently being investigated.

ACKNOWLEDGMENTS

The authors are grateful to Drs. Larry Toto, H. L. Kundel for the digitized mammographic data set. The work of the authors is supported by grants DAMD 179717271 and NS 37172.

REFERENCES

1. J.N. Wolfe, "Breast pattern as an index of risk for developing breast cancer", *AJR*, **126**, pp. 1130–1139, 1976.
2. J.N. Wolfe, "Breast parenchymal patterns and their changes with age", *Radiology*, **121**, pp. 545–552, 1976.
3. E. Warner et. al., "The risk of breast-cancer associated with mammographic parenchymal patterns: a meta-analysis of the published literature to examine the effect of method of classification", *Cancer Detection and Prevention*, **16**, pp. 67–72, 1992.
4. A.M. Oza and N.F. Boyd, "Mammographic parenchymal patterns: a marker of breast cancer risk", *Epidemiologic Reviews*, **15**, pp. 196–208, 1993.
5. J.N. Wolfe, "Risk for breast cancer development determined by mammographic parenchymal pattern", *Cancer*, **37**, pp. 2486–92, 1976.
6. M. Moscowitz, P. Gartside and C. McLaughlin, "Mammographic patterns as markers for high-risk benign breast disease and incident cancers", *Radiology*, **134**, pp. 293–5, 1980.
7. N.F. Boyd et. al., "Quantitative classification of mammographic densities and breast cancer risk: results from the Canadian national breast screening study", *Journal of the National Cancer Institute* **87**, pp. 670–675, 1995.
8. J.N. Wolfe, A.F. Saftlas and M. Salane, "Mammographic parenchymal patterns and quantitative evaluation of mammographic densities: a case control study", *American Journal of Roentgenology*, **148**, pp. 1087–92, 1987.
9. J. K. Udupa, L. Wei, Y. Miki, and R. I. Grossman, "A system form comprehensive analysis of multiple sclerosis lesion load based on MR imagery", *SPIE Proceeding*, **3031**, pp. 610–618, 1997.
10. J. K. Udupa, L. Wei, S. Samarasekera, Y. Miki, M. A. van Buchem, and R. I. Grossman, "Multiple sclerosis lesion quantification using fuzzy connectedness principles", *IEEE Medical Imaging*, **16**, pp. 598–609, 1997.
11. Y. Mike, R.I Grossman, S. Samarasekera, J.K. Udupa, M.A. van Buchem, B.S. Cooney, S.N. Pollack, D.L. Kolson, M. Polansky, L.J Mannon, "Clinical correlation of computer assisted enhancing lesion quantification in multiple sclerosis", *American Journal of Neuroradiology*, **18**, pp. 705–710, 1997.
12. Y. Miki, R.I Grossman, J.K. Udupa, L. Wei, D.L. Kolson, L.J Mannon, "Isolated U-fiber involvement in MS: preliminary observations", *Neurology*, **50**, pp. 1301–1306, 1998.
13. A. Kumar, W. Bilker, J.K. Udupa, G. Gottlieb, "Late onset minor and major early evidence for common neuroanatomical substrates detected by using MRI", proceedings of the *National Academy of Science*, **95**, pp. 7654–7658, 1998.
14. J. K. Udupa, D. Odhner, J. Tian, G. Holland, and L. Axel, "Automatic clutter-free volume rendering for MR angiography using fuzzy connectedness", *SPIE Proceeding*, **3034**, pp. 111–119, 1997.

15. J.K. Udupa, J. Tian, D.C. Hemmy, P. Tessier, "A pentium-based craniofacial 3D imaging and analysis system", *Journal of Craniofacial Surgery*, **8**, pp. 333–339, 1997.
16. S.M. Lippman, T.L. Bassford and F.L. Meyskens, Jr., "A quantitatively scored cancer-risk assessment tool: its development and use", *Journal of cancer Education*, **7**, pp. 15–36, 1992.
17. R.T. Chlebowski et. al., "Breast cancer chemoprevention tamoxifen: current issues and future prospective", *Cancer* **72**, pp. 1032–7 Supplement, 1993.
18. J. M Boone, K. K. Lindfors, C. S. Beatty, and J. A. Selbert, "A breast density index for digital mammograms based on radiologists' ranking", *Journal of Digital Imaging*, **11**, pp. 101–115, 1998.
19. J. W. Byng, N. F. Boyd, L. Little, G. Lockwood, E. Fishell, R. A. Jong, and M. J. Yaffe, "Symmetry of projection in the quantitative analysis of mammographic images", *European Journal of Cancer Prevention*, **5**, pp. 319–327, 1996.
20. G. Ursin, A. Melvin, A. Astrahan, M. Salane, Y. R. Parisky, J. G. Pearce, J. R. Daniels, M. C. Pike, and D. V. Spicer, "The detection of changes in mammographic densities", *Cancer Epidemiology, Biomarkers and Prevention*, **7** pp. 43–47, 1998.
21. Z. Huo, M. L. Giger, O. I. Olopade, and S. A. Cummings, "Computerized analysis of parenchymal patterns for the assessment of breast cancer risk", *Supplement to Radiology, RSNA*, **209(P)**, pp. 354, 1998.
22. J. K. Udupa, and S. Samarasekera, "Fuzzy connectedness and object definition: theory, algorithms, and applications in image segmentation", *Graphical Models and Image Processing*, **58**, pp. 246–261, 1996.
23. P. K. Saha, J. K. Udupa, and D. Odhner, "Scale-based fuzzy connected image segmentation: theory, algorithms, and validation", Technical Report-MIPG238, Medical Image Processing Group, Department of Radiology, University of Pennsylvania, 1998, submitted to *Computer Vision and Image Understanding.*
24. J.K Udupa, D. Odhner, S. Samarasekera, R.J. Goncalves, K. Iyer, K. Venugopal, S. Furuie, "3DVIEWNIX: a open, transportable, multidimensional, multimodality, multiparametric imaging system, proceedings of *SPIE*, **2164**, pp. 58–73, 1994.
25. A.X. Falcão, J.K. Udupa, S. Samarasekera, S. Sharma, "User-steered image segmentation paradigms: live wire and live lane", *Graphical Models Image Processing* **60**, pp. 233–260, 1998.
26. M. Tabb and N. Ahuja, "Multiscale image segmentation by integrated edge and region detection", *IEEE Trans. Image Processing*, **6**, pp. 642–655, 1997.
27. T. Lindeberg, *Scale-Space Theory in Computer Vision*. Boston, MA: Kluwer, 1994.

An ultra-fast user-steered image segmentation paradigm: live-wire-on-the-fly

Alexandre X. Falcão[a], Jayaram K. Udupa[b], and Flávio K. Miyazawa[a]

[a]Computing Institute, State University of Campinas, Campinas, SP, Brazil

[b]Department of Radiology, University of Pennsylvania, Philadelphia, PA, USA

ABSTRACT

In the past, we have presented three user-steered image segmentation paradigms: live wire, live lane, and the 3D extension of the live-wire method. In this paper, we introduce an ultra-fast live-wire method, referred to as live-wire-on-the-fly, for further reducing user's time compared to live wire. For both approaches, given a slice and a 2D boundary of interest in this slice, we translate the problem of finding the best boundary segment between any two points specified by the user on this boundary to the problem of finding the minimum-cost path between two vertices in a weighted and directed graph. The entire 2D boundary is identified as a set of consecutive boundary segments, each specified and detected in this fashion. A drawback in live wire is that the speed for optimal path computation depends on image size, compromising the overall segmentation efficiency. In this work, we solve this problem by exploiting some properties of graph theory to avoid unnecessary minimum-cost path computation during segmentation. Based on 164 segmentation experiments from an actual medical application, we demonstrate that live-wire-on-the-fly is about 1.5 to 33 times faster than live wire for actual segmentation, although the pure computational part alone is found to be over a hundred times faster.

Keywords: image segmentation, boundary detection, active boundaries, 3D imaging, shortest-path algorithms, dynamic programming, graph theory.

1. INTRODUCTION

Image segmentation is a hard problem with numerous applications in the imaging sciences.[1] It consists of two tightly coupled tasks - *recognition* and *delineation*. Recognition is the process of identifying roughly the whereabouts of a particular object in the image and delineation is the process of specifying the precise spatial extent and composition of this object. While computer algorithms are very effective in object delineation, the absence of relevant global object-related knowledge is the main reason for their failure in object recognition. On the other hand, a simple user assistance in object recognition is often sufficient to complement this deficiency and to complete the segmentation process. There are many difficult segmentation tasks that require a detailed user assistance. To address these problems, a variety of interactive segmentation methods are being developed.[2] These methods range from totally manual painting of object regions or drawing of object boundaries to the detection of object region/boundaries with minimal user assistance.[3–7]

We have been developing interactive segmentation strategies with two specific aims: (i) to provide as *complete* a *control* as possible to the user on the segmentation process *while* it is being executed, and (ii) to minimize the user involvement and the total user's time required for segmentation, without compromising the precision and accuracy of segmentation. Our strategy in these methods has been to actively exploit the superior abilities of human operators (compared to computer algorithms) in object recognition and the superior abilities of computer algorithms (compared to human operators) in object delineation.

In the past, we have presented two user-steered segmentation paradigms, referred to as live wire and live lane,[6,8] to segment 3D/4D object boundaries in a slice-by-slice fashion. These methods are in routine use in two applications[9–12] with over 15,000 tracings done so far. Although the live-wire method has its origin in some early joint work between Barrett and Udupa,[13–15] this method has been subsequently developed independently by the two groups.[6–8,16–18] There are many differences between the live-wire method developed by each group, as previously explained in.[6] Besides these differences, we have extended the ideas underlying the live-wire method to create new methods, live

Further author information: Send correspondence to A.X.F.: E-mail:afalcao@dcc.unicamp.br, Telephone: +55(19)7885881, FAX +55(19)7885847.

lane[6] and the 3D extension of live wire.[16] In this paper, we introduce an ultra-fast live-wire method, referred to as live-wire-on-the-fly, with a new live-wire algorithm for drastically reducing user's time compared to our previous work on 2D live wire.

In live wire,[6,7] to segment a 2D boundary, the user initially picks a point on the boundary and all possible minimum-cost paths from this point to all other points in the image are computed via dynamic programming. Subsequently, a "live wire" is displayed in real time from the initial point to any subsequent position taken by the cursor. If the cursor is close to the desired boundary, the live wire snaps on to the boundary. The cursor is then deposited and a new live-wire segment is found next. The entire 2D boundary is specified via a set of live-wire segments in this fashion. A drawback of this approach is the computational time for all possible minimum-cost segments from each selected point on the boundary to other points in the image. This time increases with the size of the image compromising the interactivity of the method in some practical situations. For images from 256×256 to 1024×1024 pixels, for example, live wire running on a 300MHz Pentium PC requires about 2 to 180 seconds to compute all possible minimum-cost segments from each selected point.

In live wire on the fly, the user-interaction process remains the same, but we have devised a linear time complexity algorithm to save a considerable amount of user time by avoiding the computation of all possible minimum-cost segments. When the user selects a point on the boundary, the live-wire segment is *computed and displayed* in real time from the selected point to any subsequent position of the cursor in the image. To make this feasible, we exploit the fact that by the time we have found a live-wire segment with cost value K, we have actually found all possible live-wire segments with cost value less than K in the image. Moreover, any live-wire segment with cost value greater than or equal to K contains one of the previous live-wire segments with cost value less than K. Therefore, the computation of the minimum-cost segment from a selected point to the current position of the cursor uses the results of computation from the selected point to the previous position of the cursor.

In Section 2, we present the live-wire-on-the-fly method and its algorithms. In Section 3, we present the results of evaluation between live wire and live wire on the fly based on efficiency for segmentation. Finally, we state some concluding remarks in Section 4.

2. LIVE-WIRE-ON-THE-FLY

We define a *2D scene* $\mathbf{C}$ as a pair (C, g) consisting of a finite 2D rectangular array C of pixels and a function $g(p) : C \rightarrow [L, H]$ that assigns to each pixel p in C an intensity value lying in an interval $[L, H]$. We associate with C a directed graph in which the vertices of the pixels represent the nodes of the graph and the oriented pixel edges represent the arcs. A 2D boundary of interest in $\mathbf{C}$ is a closed, oriented, and connected contour made up of oriented pixel edges. Each oriented pixel edge in $\mathbf{C}$ is a potential boundary element b, which is called a *bel* for short. To each bel b, we assign a set of features whose values characterize the "boundariness" of b. These values are converted to a single joint cost value $c(b)$ per bel b. Thus, the problem of finding the best boundary segment (live-wire segment) between any two points (pixel vertices) specified on the boundary is translated to finding the minimum-cost path between the corresponding two vertices of the graph. The issues about selection of features and how to convert feature values into cost values were previously addressed in.[6] The problem we want to address here is how to reduce the time for optimum path computation, and, consequently, the total user's time required for segmentation.

To tackle this problem, we will exploit some known properties of graph theory, particularly for the computation of shortest-paths, as described in Section 2.1. This leads to the algorithms presented in Section 2.2.

2.1. Graph Properties of Shortest Paths

In the literature on shortest-path algorithms,[19] there are many efficient solutions for finding minimum-cost paths in a weighted and directed graph. Particularly, we have adopted Dial's implementation of the Dijkstra's algorithm.[20] This algorithm computes the shortest-paths to all nodes from a single node in $O(m + nC)$ time, where m is the number of arcs, n is the number of nodes, and C is the maximum cost assigned to any arc in the graph. Actually, in this case, the cost assigned to each arc should be an integer in the interval $[0, C]$. Dial's solution uses a circular queue with $C + 1$ buckets of nodes as the priority queue of the Dijkstra's algorithm. Since the bottleneck of the Dijkstra's algorithm is in maintaining the priority queue, Dial's solution uses the bucket sort algorithm to speed up this process. We will come back to this issue in Section 2.2.

In our problem, the live-wire segment between a selected point v_s on the boundary and the current position v_e of the cursor in $\mathbf{C}$ is the shortest-path $P = (v_s \rightsquigarrow v_e)$ from v_s to v_e in our graph, where the cost of P, denoted

$K(P)$, is the sum of the joint costs $c(b)$ of all bels b comprising P. In fact, Dijkstra's algorithm returns a tree of minimum-cost path (or a tree of shortest-path) rooted at v_s,[21] which consists of all minimum-cost paths from v_s to all vertices in $\mathbf{C}$. We will denote this tree by $T(v_s) = \{P = (v_s \rightsquigarrow v_e)/v_e \in \mathbf{C}\}$.

For any real number k, we denote by $T_k(v_s)$ the tree of minimum-cost path rooted at v_s such that the cost of any path in this tree is less than k. That is, $T_k(v_s) = \{P = (v_s \rightsquigarrow v_e)/v_e \in \mathbf{C}, K(P) < k\}$. The algorithm reported in this paper exploits the following properties of $T(v_s)$.

1. To compute the minimum-cost path $P = (v_s \rightsquigarrow v_e)$ with cost $K(P)$, there is no need to compute $T_k(v_s)$ for $k > K(P)$.
2. By the time we have found the minimum-cost path $P = (v_s \rightsquigarrow v_e)$ with cost $K(P)$, we have actually found the tree of minimum-cost path $T_{K(P)}(v_s)$.
3. The tree of minimum-cost path $T_k(v_s)$ contains the tree of minimum-cost path $T_{K(P)}(v_s)$ whenever $k \geq K(P)$.

We use the first property to modify Dial's implementation of the Dijkstra's algorithm to quit optimum path computation by the time we have found the minimum-cost path $P = (v_s \rightsquigarrow v_e)$. We call this algorithm DSP (see Section 2.2). We use the second property to avoid optimum path computation for any path $P' = (v_s \rightsquigarrow v'_e)$ with cost $K(P') < K(P)$. Thus, when the user moves the cursor to a new position v'_e, such that $K(P') < K(P)$, and we have already found P, the algorithm just shows $P' = (v_s \rightsquigarrow v'_e)$ without requiring computation. We use the third property to continue optimum path computation for paths $P' = (v_s \rightsquigarrow v'_e)$ with costs $K(P') \geq K(P)$ based on the previous result of algorithm DSP for computing P.

2.2. ALGORITHMS

Algorithm LWOF

Input: The joint cost function c and an initial vertex v_0 selected on a 2D boundary of interest in $\mathbf{C}$;
Output: A closed, connected, and oriented contour $\mathbf{B}$ (made up of bels);
Auxiliary Data Structures: A 2D "cumulative cost" array *cc* representing the total cost of the optimal paths found so far from v_s to other vertices in $\mathbf{C}$; a 2D "direction" array *dir* indicating, for each vertex, to which of its immediate neighboring vertices the optimal path goes; a circular queue Q of vertices with $C+1$ buckets; a list L of vertices which have already been processed; a current path $P(v_s \rightsquigarrow v_e)$, where v_s is the current point selected on the boundary and v_e is the current position of the cursor in $\mathbf{C}$; and a list $\mathbf{B}$ of bels which have already been identified as belonging to the boundary of interest in $\mathbf{C}$;

begin

1. set $cc(v)$ to ∞ and $dir(v)$ to *null* for all vertices v in $\mathbf{C}$, and set L to empty;
2. $v_s \leftarrow v_0$, set $cc(v_s)$ to 0, and put v_s in Q;
3. *repeat*
   a. determine the vertex v_e in $\mathbf{C}$ pointed to by the cursor;
   b. if v_e is not a vertex of any bel in $\mathbf{B}$ *then*
      (i) compute $P \leftarrow$DSP$(v_s, v_e, Q, cc, c, dir, L)$ and display the bels in P;
      (ii) *if* v_e is selected by the user and $v_e \in \mathbf{C}$ *then*
         a. add the bels in P to $\mathbf{B}$;
         b. set $cc(v)$ to ∞ and $dir(v)$ to *null* for all vertices v in $\mathbf{C}$;
         c. remove all vertices v from Q, and remove from L all vertices v which do not belong to any bel in $\mathbf{B}$;
         d. $v_s \leftarrow v_e$, set $cc(v_s)$ to 0, remove v_s from L, and put v_s in Q;

endif;

endif;

until the user indicates a "close" operation;

4. $v_e \leftarrow v_0$ and remove v_e from L;
5. compute $P \leftarrow$DSP$(v_s, v_e, Q, cc, c, dir. L)$ and display the bels in P;
6. add the bels in P to $\mathbf{B}$ and output the bels in $\mathbf{B}$;

end

Algorithm DSP

Input: an initial vertex v_s; a terminal vertex v_e; the circular queue Q; the cumulative cost array cc; the joint cost function c; the direction array dir: and the list L of already processed vertices;
Output: A set of bels forming an optimal path from v_s to v_e;

begin

1. *while* $v_e \notin L$ *do*
   a. remove a vertex v from Q such that $cc(v) = \min_{v' \in Q}\{cc(v')\}$, and put v in L;
   b. *for* each vertex v' such that v' is in the set of the 4-adjacent neighbors of v and $v' \notin L$ *do*
      (i) compute $cc_{tmp} = cc(v) + c(b')$ where b' is the bel whose direction goes from v' to v and $c(b')$ is the joint cost of b';
      (ii) *if* $cc_{tmp} < cc(v')$ *then*
         a. set $cc(v')$ to cc_{tmp} and $dir(v')$ to the direction from v' to v;
         b. *if* $v' \notin Q$ *then* insert v' in Q *else* update v' in Q;
      endif;
   endfor;

   endwhile;
2. starting from v_e, trace recursively the next vertex pointed to by the current vertex using the direction information in dir until v_s is reached, and return the bels so traced;

end

In the algorithms above, Q is a bucket represented by a circular vector with $C + 1$ positions from 0 to C (see Figure 1). Each position i, $i = 0, \ldots, C$, has associated with it a doubly linked list which contains vertices with the same cumulative cost value. In Step 3b(ii)c of algorithm LWOF, we remove all vertices v from Q in $O(C)$ time since we just have to set to *null* the list associated with each position i, $i = 0, \ldots, C$, in Q. An index i_0 is used to indicate the current initial position in Q (see Figure 1). In Step 1a of algorithm DSP, a vertex v in Q with the minimum cumulative cost $cc(v)$ is removed from the beginning of the doubly linked list at position i_0. If this list is empty, i_0 is incremented until the next position in which a non-empty list is found. Taking the worst case, this operation has a computational time complexity of $O(C)$. In Step 1b(ii)b of algorithm DSP, a vertex v' with cumulative cost $cc(v')$ is inserted in Q at the beginning of the doubly linked list at position $[cc(v') \bmod (C + 1)]$. This operation has a computational time complexity of $O(1)$. The Dijkstra's algorithm guarantees that the vertices in Q will be always stored in the increasing order of cumulative cost, because the difference between the maximum and the minimum

cumulative costs of the vertices in Q is always less than or equal to C. In the same step, a vertex v' in Q may have its cumulative cost updated, meaning that we have found a new path from v_s to v' with a cost less than the current cost $cc(v')$. In this case, we have to remove v' from its current position in Q and insert it into a new position in Q. This process is done with a computational time complexity of $O(1)$.

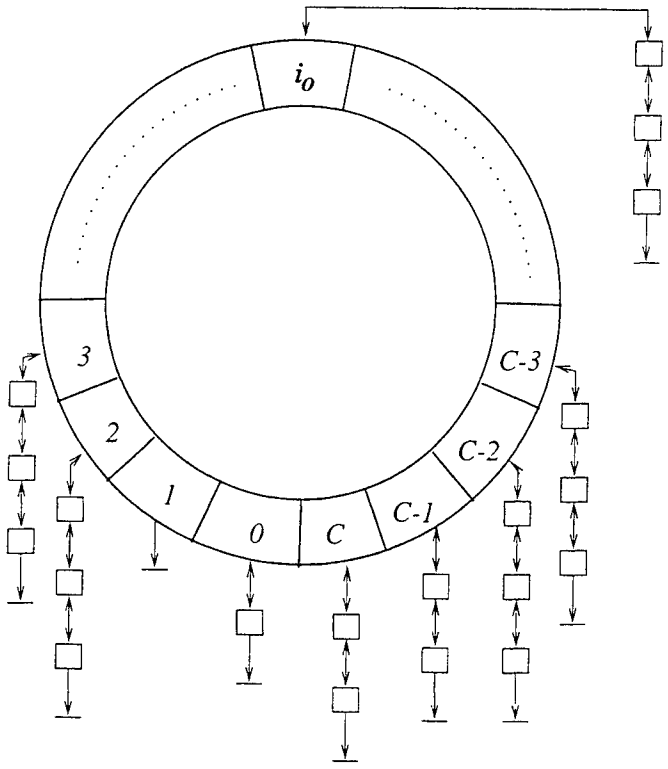

Figure 1. Bucket Structure in a *circular* queue.

In the worst case, algorithm DSP has the same computational time complexity $O(m + nC)$ as in the Dial's implementation of Dijkstra's algorithm, where m is the number of bels in $\mathbf{C}$, n is the number of vertices in $\mathbf{C}$ and C is the maximum cost $c(b)$ assigned to any bel b. Other shortest-path algorithms exist with computational time complexity less than $O(m+nC)$ (e.g., $O(m+n\log C)$, $O(m+n\sqrt{\log C})$, and $O(m\log\log C)$, see[20]). These algorithms use more complex data structures than our circular queue to reduce the time complexity for inserting and removing vertices. In our implementation, we have a time complexity of $O(1)$ for inserting and updating vertices in Q. In the worst case, we have a time complexity of $O(C)$ for removing a vertex from Q with minimum cumulative cost, as opposed to a logarithmic complexity obtained by these algorithms. After some experimentation, we have found that the number of increments to reach the next non-empty position in Q is usually less than 0.01 of C. Actually, even C is not a big number. Typically, we have used 4095 and 255 for C in our implementation of live wire. Therefore, it is not clear that the speed improvement in live wire with other algorithms is really significant. This should be investigated further.

3. EVALUATION

In,[6] we have assessed the goodness of a segmentation method based on three factors - precision, accuracy, and efficiency. Precision refers to the repeatability of the method and can be measured by evaluating the variations in the result of segmentation because of subjective operator input. Accuracy refers to the degree of agreement with truth. Efficiency refers to the practical viability of the method expressed as some function of the total user's time required to complete the segmentation process. Based on 2,000 tracings in a particular application and statistical analysis of the results, we have shown that the segmentations of the 2D live-wire method in general agree with those of manual tracing (accuracy) and that the live-wire method is more repeatable (precision), with a statistical

significance level of $p < 0.03$, and 1.5-2.5 times faster (efficiency), with a statistical significance level of $p < 0.02$, than the manual method. In this section, we will show the results of comparing live wire and live wire on the fly taking into account the efficiency of the methods. Since the delineation of the contours output by live wire on the fly is exactly in the same way as in live wire, the accuracy and precision of the former will be identical to those of the latter, and, therefore, they need not be assessed again.

In,[6] we have introduced a feature called f_8 in live wire to constrain the search for optimal paths in the current slice to an annular region (shell) of width W centered around the projection onto the current slice of the contour(s) traced in the previous slice. With feature f_8, live wire yields very fast response even for large images. Of course, we can also use f_8 to further improve the efficiency of live wire on the fly on large images, but we will consider in this section a comparison between live wire with f_8 and live wire on the fly. Therefore, our experiments will take into account three methods:

- LW: live wire without f_8.
- LWF8: live wire with f_8 using $W = 60$ pixels.
- LWOF: live wire on the fly.

For our experiments, we have chosen one object (the talus bone of the human foot) in one of our ongoing applications, the kinematic analysis of the tarsal joints of the foot based on MR images.[9–11] This was one of the objects used in the past to evaluate the previous live methods.[6,16] We created a set of 67 2D scenes from the images within our database as follows. The images (slices) in our database are all of size 256 × 256 pixels. We chose a set, denoted $\mathbf{C}_{256}$, of 30 slices from this set pertaining to the data set of one subject. By bilinear interpolation of each of these slices, we created another set, denoted $\mathbf{C}_{128}$, of 30 128 × 128 slices. Analogously, we created a set $\mathbf{C}_{512}$ of five 512 × 512 slices and a set $\mathbf{C}_{1024}$ of two 1024 × 1024 slices from the original 256 × 256 slices. The reason for choosing a fewer number of scenes of size 512×512 and 1024×1024 is that the response time of LW in these scenes is prohibitively slow. One operator segmented the talus in each of these scenes using each of the two methods LW and LWOF. He also segmented the talus in $\mathbf{C}_{256}$ using LWF8. Our evaluation study thus consists of 164 segmentation experiments in total. More experiments involving other operators are currently underway. We used a 300 MHz Pentium PC for these experiments.

We denote the *time taken* to complete any segmentation experiment e by T_e (expressed in seconds). Consider any fixed scene type $t \in \{\mathbf{C}_{128}, \mathbf{C}_{256}, \mathbf{C}_{512}, \mathbf{C}_{1024}\}$ and method $m \in \{\text{LW, LWOF, LWF8}\}$. We define the *time taken* T_{tm} (in seconds/slice) for segmenting the talus in a 2D scene of type t using method m to be the average of all times T_e over all segmentation experiments e involving m and all 2D scenes of type t.

We have done three types of timing measurements. The first type measures the CPU times for computing the live wire segments independent of other supporting processes that are required to conduct live wire segmentation. This allows us to assess the difference in speed that exists purely between the old and the new algorithms. The second type measures the time taken by the user to segment one complete contour ignoring the time for other processes such as displaying the slice and the computation of the cost values $c(b)$ for all bels. The third type includes all processes, and, therefore, gives an idea of the comparative user time required for overall segmentation for the different methods in an actual application. We note here that, as in the live-wire method,[6] training is required only once for an application and is not needed on a per study basis. This is typically under 5 minutes and is not included in any of the time measurements.

Tables 1, 2 and 3 list the values of T_{tm} for all possible values of t and m, for the three types of measures, respectively. Although $LWOF$ can find optimum paths hundreds of times faster than LW (see Table 1), users cannot react with the same speed (see Table 2). Table 3 shows that, from the point of view of actual segmentation, $LWOF$ is about 1.5 to 33 times faster than LW for images from 128 × 128 pixels to 1024 × 1024 pixels. Even constraining optimum path computation into an anular region of width equal to 60 pixels (i.e., method $LWF8$), live wire on the fly is about 2.3 times faster. Note that, the advantage of live wire on the fly over live wire increases with the size of the image and with the number of points required per boundary. In our experiments, the 2D boundaries of the talus require 2 to 5 points in both live wire strategies.

	C_{128}	C_{256}	C_{512}	C_{1024}
LW	2.14	15.17	99.57	901.24
LWOF	0.23	0.62	2.27	8.74
LWF8	–	8.25	–	–

Table 1. Segmentation times T_{tm} in seconds/slice for all possible values of t and m. This table lists the first type of measurement that indicates the time taken by the shortest-path algorithms only independent of other processes.

	C_{128}	C_{256}	C_{512}	C_{1024}
LW	8.37	20.93	116.20	959.00
LWOF	5.67	5.33	8.00	15.50
LWF8	–	14.13	–	–

Table 2. Segmentation times T_{tm} in seconds/slice for all possible values of t and m. This table lists the second type of measurement that indicates the time taken by the user to segment one complete contour ignoring the time for other processes.

	C_{128}	C_{256}	C_{512}	C_{1024}
LW	12	24	120	990
LWOF	8	8	12	30
LWF8	–	18	–	–

Table 3. Segmentation times T_{tm} in seconds/slice for all possible values of t and m. This table lists the third type of measurement that indicates the time taken by the user for overall segmentation including all processes.

4. CONCLUDING REMARKS

We have presented a new user-steered image segmentation paradigm, called live wire on the fly, to segment 3D/4D object boundaries in a slice-by-slice fashion. The method uses the previously published live wire framework,[6] but utilizes a substantially faster shortest-path algorithm for improving speed. Based on 164 segmentation experiments from an actual medical application, we have shown that the new method is about 1.5 to 33 times faster than live wire for actual segmentation, although the pure computational part alone is over a hundred times faster. Other experiments involving multiple operators are being done.

A drawback of live wire is the computation time for all possible minimum-cost segments from each selected point on the boundary to all other points in the image. This time increases with the size of the image compromising the interactivity of the method in some practical situations. Tables 1- 3 show that live wire loses efficiency considerably for images larger than 256 × 256 pixels. We have eliminated this problem in live wire on the fly by avoiding unnecessary optimum path computation during the segmentation process. Thus, live wire on the fly computes and displays live-wire segments in real time, even for very large images, even on low-powered computers.

ACKNOWLEDGMENTS

The work of the first author (A.X.F.) was partially supported by FAPESP (Proc. 98/06314-5 and Proc. 97/13306-6). The research of the second author is supported by an NIH grant NS 37172 and a grant DAMD 179717271 from the Department of Army. The third author (F.K.M.) has been partially supported by Project ProNEx 107/97 (MCT/FINEP) and CNPq individual research grants: Proc. 300301/98-7.

REFERENCES

1. R.M. Haralick and L.G. Shapiro, Image segmentation techniques, *Computer Vision Graphics and Image Processing*, vol. 29, no. 1, pp. 100-132, Jan, 1985.
2. S.D. Olabarriaga and A.W.M. Smeulders, Setting the mind for intelligent interactive segmentation: Overview, requirements, and framework, *Lecture Notes on Computer Science*, vol. 1230, pp. 417-422, 1997.
3. W.E. Higgins and E.J. Ojard, Interactive morphological watershed analysis for 3D medical images, *Computerized Medical Imaging and Graphics*, vol. 17, no. 4/5, pp. 387–395, 1993.
4. R. Adams and L. Bischof, Seeded Region Growing, *IEEE Transactions on Pattern Analysis and Machine Intelligence*, vol. 16, no. 6, pp 641–647, Jun, 1994.
5. T. McInerney and D. Terzopoulos, Deformable models in medical image analysis: A survey, *Medical Image Analysis*, vol. 1, no. 2, pp. 91-108, 1996.
6. A.X. Falcão, J.K. Udupa, S. Samarasekera, S. Sharma, B.E. Hirsch, and R.A. Lotufo, User-steered image segmentation paradigms: live-wire and live-lane, *Graphical Models and Image Processing*, vol. 60, no. 4, pp. 233-260, Jul, 1998.
7. E.N. Mortensen and W.A. Barrett, Interactive segmentation with intelligent scissors. *Graphical Models and Image Processing*, vol. 60, no. 5, pp. 349-384, Sep, 1998.
8. A.X. Falcão, J.K. Udupa, S. Samarasekera and B.E. Hirsch, User-steered image boundary segmentation, in *Proceedings of SPIE on Medical Imaging*, Newport Beach, CA, vol. 2710, pp. 278-288, Feb, 1996.
9. J.K. Udupa, B.E. Hirsch, S. Samarasekera, H. Hillstrom, G. Bauer, and B. Kneeland, Analysis of in vivo 3D internal kinematics of the joints of the foot, *IEEE Transactions on Biomedical Engineering*, vol. 45, pp. 1387-1396, 1998.
10. B.E. Hirsch, J.K. Udupa, and S. Samarasekera, A new method of studying joint kinematics from 3D reconstructions of MRI data, *Journal of the American Podiatric Medical Association*, vol. 86, no. 1, pp. 4-15, 1996.
11. E. Stindel, J.K. Udupa, B.E. Hirsch, D. Odhner, and C. Couture, 3D MR image analysis of the morphology of the rear foot: Application to classification of bones, *Journal of Bone and Joint Surgery*, submitted.
12. R.C. Rhoad, J.J. Klimkiewicz, G.R. Williams, S.B. Kesmodel, J.K. Udupa, B. Kneeland, and J.P. Iannotti, A new in vivo technique for 3D shoulder kinematics analysis, *Skeletal Radiology*, vol. 27, pp. 92-97, 1998.
13. B.S. Morse, W.A. Barrett, J.K. Udupa, and R.P. Burton, Trainable optimal boundary finding using two-dimensional dynamic programming, *Technical Report MIPG180*, Medical Image Processing Group, Department of Radiology, University of Pennsylvania, Mar, 1991.
14. J.K. Udupa, S. Samarasekera, W.A. Barrett, Boundary detection via dynamic programming, in *Proceedings of SPIE*, vol. 1808, pp. 33-39, 1992.
15. E.N. Mortensen, B.S. Morse, W.A. Barrett and J.K. Udupa, Adaptive boundary detection using live-wire two dimensional dynamic programming, in *IEEE Proceedings of Computers in Cardiology*, pp. 635-638, Oct, 1992.
16. A.X. Falcão and J.K. Udupa, Segmentation of 3D objects using live-wire, in *Proceedings of SPIE on Medical Imaging*, Newport Beach, C, vol. 3034, pp. 228-239, Feb, 1997.
17. E.N. Mortensen and W.A. Barrett, Intelligent scissors for image composition, in *Proceedings of Computer Graphics (SIGGRAPH'95)*, Los Angeles, C, pp. 191-198, Aug, 1995.
18. W.A. Barrett and E.N. Mortensen, Fast, accurate, and reproducible live-wire boundary extraction, *in Proceedings of Visualization in Biomedical Computing*, Hamburg, Germany, pp. 183-192, Sep, 1996.
19. N. Deo and C. Pang, Shortest-path algorithms: Taxonomy and annotation, *Networks*, vol. 14, pp. 275-323, 1984.
20. R.K. Ahuja, T.L. Magnanti and J.B. Orlin, Network Flows: Theory, Algorithms and Applications, *Prentice-Hall*, Englewood Cliffs, NJ, 1993.
21. R.E. Tarjan, Data Structures and Network Algorithms, *Society for Industrial and Applied Mathematics*, Philadelphia, PA, 1983 (sixth printing in 1991).